Supporting Information for "Magnetic Induction Responses of Jupiter's Ocean Moons Including Effects from Adiabatic Convection"

S. D. Vance[1], B. G. Bills[1], C. J. Cochrane[1], K. M. Soderlund[2],

N. Gómez-Pérez[3], M. J. Styczinski[4], and C. Paty[5]

[1]Jet Propulsion Laboratory, California Institute of Technology, Pasadena, USA

[2]Institute for Geophysics, John A. & Katherine G. Jackson School of Geosciences, The University of Texas at Austin, USA

[3]British Geological Survey, Edinburgh, UK

[4]Dept. of Physics, University of Washington, Seattle, USA

[5]Dept. of Earth Sciences, University of Oregon, Eugene, USA

Contents of this file

Text S1. Induction response model

We are interested in the magnetic fields induced within a spherically symmetric body, in which electrical conductivity is a piece-wise constant function of distance from the center. We thus assume bounding radii for N layers

$$\{r_1, r_2, r_3, \cdots, r_N\} \tag{S1}$$

where

$$r_N = R \tag{S2}$$

is the outer radius of the spherical body.

The corresponding conductivity values are

$$\{\sigma_1, \sigma_2, \sigma_3, \cdots, \sigma_N\} \tag{S3}$$

We also assume that there is an imposed external magnetic potential, represented by a sum of terms, each of which has the form

$$\Phi_{n,m,p}(r, \theta, \varphi, t) = RB_e \left(\frac{r}{R}\right)^n S_{n,m}(\theta, \varphi) \mathrm{e}^{-i\omega_p t} \tag{S4}$$

where $\{r, \theta, \varphi\}$ are spherical coordinates (r is radius, θ is colatitude, and φ is longitude) of the field point, B_e is a scale factor, $S_{n,m}(\theta, \varphi)$ is a surface spherical harmonic function of degree n and order m, while t is time and ω_p is the angular frequency of oscillation of the imposed potential. The same methods apply independently to each frequency ω_p in the excitation field, and the results sum linearly by superposition. Therefore, we now drop the subscript on this quantity and simply use ω.

Within each layer, the magnetic field vector $\mathbf{B}$ must satisfy the Helmholtz equation

$$\nabla^2 \mathbf{B} = -k^2 \mathbf{B} \tag{S5}$$

which is a diffusion equation for $\mathbf{B}$. k is a scalar wavenumber given by

$$k^2 = i\omega\mu_0\sigma \tag{S6}$$

where ω is angular frequency, σ is electrical conductivity, and the magnetic constant (permeability of free space) is given by

$$\mu_0 = 4\pi \times 10^{-7} N/A^2 \tag{S7}$$

with units N and A being Newton and Ampere. In defining k in Equation S6, we have assumed $\mu \approx \mu_0$, which holds well even for ferromagnetic materials when they are considered on a global scale (Saur et al., 2009). Note that in Equation S6, we have chosen a different convention from that of Parkinson (1983) and numerous authors relying on their derivation. We make this choice in order to derive the spherical Bessel equation (Equation S11) from the diffusion equation (5). Choosing $k^2 = -i\omega\mu_0\sigma$ results in the *modified* spherical Bessel equation, meaning the derivation in Parkinson (1983) is in error. We prefer to define k^2 as in Equation S6 so that we can, in fact, reach the spherical Bessel equation and thereby compare the remaining derivation favorably to that of Parkinson (1983) and other past research using the standard spherical Bessel functions.

Independently from Equation S5, the net poloidal component of the magnetic field inside the body is given by sums over n and m of terms with the forms

$$B_r(r,\theta,\varphi,t) = \frac{C}{r}\Big(F(r)\Big)n(n+1)\ S_{n,m}(\theta,\varphi)\mathrm{e}^{-i\omega t} \tag{S8}$$

$$B_\theta(r,\theta,\varphi,t) = \frac{C}{r}\frac{d}{dr}\Big(rF(r)\Big)\ \frac{d}{d\theta}\Big(S_{n,m}(\theta,\varphi)\Big)\mathrm{e}^{-i\omega t} \tag{S9}$$

$$B_\varphi(r,\theta,\varphi,t) = \frac{C}{r\sin\theta}\frac{d}{dr}\Big(rF(r)\Big)\ \frac{d}{d\varphi}\Big(S_{n,m}(\theta,\varphi)\Big)\mathrm{e}^{-i\omega t} \tag{S10}$$

where C is a constant, and $F(r)$ is a function of radius, which we need to determine.

S1.1 Analytical model based on Srivastava (1966)

For the purpose of validating our numerical model, we separately derive an analytical solution akin to that of Srivastava (1966) and summarized by Parkinson (1983). As this analytical approach is common throughout the literature, we later compare the analytical (layered) approach to our numerical (ordinary differential equation, ODE) approach in Figures S1 and S2. We find it instructive to compare the point in the derivation where the two approaches differ, so we carry out the full derivation here, in our notation.

Applying separation of variables to the governing differential equation (Equation S5), one finds that the radial factor $F(r)$ in the solution must satisfy the spherical Bessel equation

$$\frac{d^2F}{dr^2} + \left(\frac{2}{r}\right)\frac{dF}{dr} + \left(k^2 - \frac{n(n+1)}{r^2}\right)F = 0 \tag{S11}$$

This is a second-order equation, having two solutions, $j_n(kr)$ and $y_n(kr)$, the spherical Bessel functions of the first and second kind, respectively, of degree n and argument kr.

Note that choosing to define k as we did in Equation S6 was a strict requirement to obtain Equation S11. If we instead chose $k^2 = -i\omega\mu_o\sigma$, we would have obtained the *modified* spherical Bessel equation

$$\frac{d^2F}{dr^2} + \left(\frac{2}{r}\right)\frac{dF}{dr} + \left(-k^2 - \frac{n(n+1)}{r^2}\right)F = 0 \tag{S12}$$

with solutions $i_n(kr)$ and $k_n(kr)$, the *modified* spherical Bessel functions, as in Schilling et al. (2007) and ? (?). In effect, our choice of sign convention results in the complex response we later derive $\mathcal{A}_n^e$ (Equation S46) being equal to the complex conjugate of the analogous quantity $Ae^{i\phi}$ appearing in past research (e.g., Zimmer et al., 2000).

It will also be convenient to define another set of related functions

$$F^\star(r) = \frac{d}{dr}\Big(rF(r)\Big) \tag{S13}$$

with

$$\begin{aligned} j_n^\star(kr) &= \frac{d}{dr}\Big(rj_n(kr)\Big) \\ &= (n+1)j_n(kr) - kr\, j_{n+1}(kr) \end{aligned} \tag{S14}$$

and

$$\begin{aligned} y_n^\star(kr) &= \frac{d}{dr}\Big(ry_n(kr)\Big) \\ &= (n+1)y_n(kr) - kr\, y_{n+1}(kr) \end{aligned} \tag{S15}$$

Both y_n and $y_n^\star$ are singular at the origin $r = 0$, so in the innermost spherical layer only $j_n(kr)$ and $j_n^\star(kr)$ may describe physically consistent solutions. In other layers, we use linear combinations of j_n and y_n and linear combinations of $j_n^\star$ and $y_n^\star$.

Text S1.1.1. Internal boundary conditions

The resulting piecewise-defined radial functions characterize the radial part of the magnetic field. The radial component has the form

$$F_n(r) = \begin{cases} c_1 j_n(k_1 r) & \text{for} \quad 0 < r \le r_1 \\ c_2 j_n(k_2 r) + d_2 y_n(k_2 r) & \text{for} \quad r_1 < r \le r_2 \\ c_3 j_n(k_3 r) + d_3 y_n(k_3 r) & \text{for} \quad r_2 < r \le r_3 \\ \\ c_{\mathrm{j}} j_n(k_{\mathrm{j}} r) + d_{\mathrm{j}} y_n(k_{\mathrm{j}} r) & \text{for} \quad r_{\mathrm{j}-1} < r \le r_{\mathrm{j}} \end{cases} \tag{S16}$$

The tangential components yield similar structure, but with all F_n, j_n, and y_n replaced by their starred counterparts.

The constants c_{j} and d_{j} are determined by continuity of radial (r) and tangential (θ, φ) components of the magnetic field across the boundaries. For each internal boundary, it must hold that

$$F_n^{\mathrm{below}}(r_{\mathrm{j}}) = F_n^{\mathrm{above}}(r_{\mathrm{j}})$$

$$c_{\mathrm{j}} j_n(k_{\mathrm{j}} r_{\mathrm{j}}) + d_{\mathrm{j}} y_n(k_{\mathrm{j}} r_{\mathrm{j}}) = c_{\mathrm{j}+1} j_n(k_{\mathrm{j}+1} r_{\mathrm{j}}) + d_{\mathrm{j}+1} y_n(k_{\mathrm{j}+1} r_{\mathrm{j}}) \tag{S17}$$

to ensure continuity of the radial component of the magnetic field, and likewise for $F_n^\star$ to ensure continuity of the tangential components. These continuity constraints yield two equations at each internal boundary, from which we can determine the layer coefficients.

The internal boundary conditions are only part of the story. In a model with N layers, we have $2N - 1$ coefficients to determine (recall that $d_1 = 0$, to avoid singular behavior at the origin), but only $N - 1$ internal boundaries, and thus only $2N - 2$ constraints. The

external boundary condition provides the additional information to make the problem evenly determined.

Using notation similar to that of Parkinson (1983, Ch. 5), we can write a recursion relation that transforms the coefficients in the j$^{\text{th}}$ layer into those for the layer above it

$$\begin{bmatrix} c_{\mathrm{j}+1} \\ d_{\mathrm{j}+1} \end{bmatrix} = T_{\mathrm{j}}(k_{\mathrm{j}}, k_{\mathrm{j}+1}, r_{\mathrm{j}}) \cdot \begin{bmatrix} c_{\mathrm{j}} \\ d_{\mathrm{j}} \end{bmatrix} \tag{S18}$$

where the transformation matrix T_{j} has elements

$$T_{\mathrm{j}}(k_{\mathrm{j}}, k_{\mathrm{j}+1}, r_{\mathrm{j}}) = \frac{1}{\alpha_{\mathrm{j}}} \begin{bmatrix} \beta_{\mathrm{j}} & \gamma_{\mathrm{j}} \\ \delta_{\mathrm{j}} & \varepsilon_{\mathrm{j}} \end{bmatrix} \tag{S19}$$

with

$$\alpha_{\mathrm{j}} = j_n(k_{\mathrm{j}+1}r_{\mathrm{j}})\, y_n^\star(k_{\mathrm{j}+1}r_{\mathrm{j}}) - y_n(k_{\mathrm{j}+1}r_{\mathrm{j}})\, j_n^\star(k_{\mathrm{j}+1}r_{\mathrm{j}}) = \frac{1}{k_{\mathrm{j}+1}r_{\mathrm{j}}} \tag{S20}$$

which is a function of the conductivity in the layer above the boundary only. The other elements depend on the conductivities on both sides of the boundary:

$$\beta_{\mathrm{j}} \;=\; j_n(k_{\mathrm{j}}r_{\mathrm{j}})\, y_n^\star(k_{\mathrm{j}+1}r_{\mathrm{j}}) - y_n(k_{\mathrm{j}+1}r_{\mathrm{j}})\, j_n^\star(k_{\mathrm{j}}r_{\mathrm{j}}) \tag{S21}$$

$$\gamma_{\mathrm{j}} \;=\; y_n(k_{\mathrm{j}}r_{\mathrm{j}})\, y_n^\star(k_{\mathrm{j}+1}r_{\mathrm{j}}) - y_n(k_{\mathrm{j}+1}r_{\mathrm{j}})\, y_n^\star(k_{\mathrm{j}}r_{\mathrm{j}}) \tag{S22}$$

and

$$\delta_{\mathrm{j}} = j_n(k_{\mathrm{j}+1}r_{\mathrm{j}})\, j_n^\star(k_{\mathrm{j}}r_{\mathrm{j}}) - j_n(k_{\mathrm{j}}r_{\mathrm{j}})\, j_n^\star(k_{\mathrm{j}+1}r_{\mathrm{j}}) \tag{S23}$$

$$\varepsilon_{\mathrm{j}} = j_n(k_{\mathrm{j}+1}r_{\mathrm{j}})\, y_n^\star(k_{\mathrm{j}}r_{\mathrm{j}}) - y_n(k_{\mathrm{j}}r_{\mathrm{j}})\, j_n^\star(k_{\mathrm{j}+1}r_{\mathrm{j}}) \tag{S24}$$

For computation, it is helpful to note that Equation S18 yields a convenient recursion relation if we define a quantity

$$\Lambda_{\mathrm{j}} = \frac{d_{\mathrm{j}}}{c_{\mathrm{j}}} \tag{S25}$$

We find that $\Lambda_{\mathrm{j}+1}$ relates to Λ_{j} by

$$\Lambda_{\mathrm{j}+1} = \frac{\delta_{\mathrm{j}} + \Lambda_{\mathrm{j}}\varepsilon_{\mathrm{j}}}{\beta_{\mathrm{j}} + \Lambda_{\mathrm{j}}\gamma_{\mathrm{j}}} \tag{S26}$$

As $d_1 = 0$, $\Lambda_1 = 0$ also for that innermost layer. Note that we define this transfer coefficient differently than do Parkinson (1983). They define the reciprocal of Λ so that Equations S26 and S40 appear to match. Our notation allows for $\Lambda_1 = 0$, rather than leaving this quantity undefined (Styczinski et al., *in progress*).

We thus start in the central spherical layer, where $\Lambda_1 = 0$, then propagate upward through the stack of layers until we have the coefficient Λ_N for the outermost (N^{th}) layer. With a piecewise model interior structure $\sigma(r)$, we compute k_{j} for the set of r_{j}. Repeated application of Equation S26 then allows us to relate the interior structure to the external boundary conditions.

Text S1.1.2. External boundary conditions

The final step is matching the external surface boundary condition. Outside the sphere, the magnetic field is represented by a scalar potential which is the sum of an imposed external contribution and an induced internal contribution. That sum has spatial dependence given by the form

$$\Phi(r,\theta,\varphi) = R\left(B_e\left(\frac{r}{R}\right)^n + B_i\left(\frac{R}{r}\right)^{n+1}\right)S_n(\theta,\varphi) \tag{S27}$$

We have now dropped the subscript m from $S_{n,m}$ because for any n, a suitable choice of axes results in $m = 0$ for both external and internal fields for the case of spherical symmetry we consider here. The vector field is obtained from the potential via

$$\mathbf{B} = -\nabla\Phi \tag{S28}$$

The radial component of the vector field, evaluated at the surface ($r = R$), is

$$B_r = -\Big(nB_e - (n+1)B_i\Big)S_n(\theta,\varphi) \tag{S29}$$

and the tangential components are

$$B_\theta = -\Big(B_e + B_i\Big)\frac{\partial S_n(\theta,\varphi)}{\partial\theta} \tag{S30}$$

and

$$B_\varphi = -\Big(B_e + B_i\Big)\frac{1}{\sin\theta}\frac{\partial S_n(\theta,\varphi)}{\partial\varphi} \tag{S31}$$

The θ and φ equations yield redundant information, so we consider only the θ equation for the tangential components.

Matching these with the corresponding interior components, as given in Equations S8–S10, but evaluated at the top of the uppermost layer, we obtain

$$-\Big(nB_e - (n+1)B_i\Big)R = n(n+1)\Big(c_N j_n(k_N R) + d_N y_n(k_N R)\Big) \tag{S32}$$

and

$$-\Big(B_e + B_i\Big)R = \Big(c_N j_n^\star(k_N R) + d_N y_n^\star(k_N R)\Big) \tag{S33}$$

From these two equations, we can relate the "Q response"

$$Q = \frac{B_i}{B_e} \tag{S34}$$

to the internal field coefficients:

$$Q = \frac{n}{n+1}\,\frac{c_N\beta_n + d_N\gamma_n}{c_N\delta_n + d_N\varepsilon_n} \tag{S35}$$

We define the parameters β_n, γ_n, δ_n, and ε_n by

$$\beta_n = j_n^\star(k_N R) - (n+1)j_n(k_N R) \tag{S36}$$

$$\gamma_n = y_n^\star(k_N R) - (n+1)y_n(k_N R) \tag{S37}$$

and

$$\delta_n = n j_n(k_N R) + j_n^\star(k_N R) \tag{S38}$$

$$\varepsilon_n = n y_n(k_N R) + j_n^\star(k_N R) \tag{S39}$$

Note that we define these quantities as above for consistency with Parkinson (1983) and for similarity between the definitions of the transfer coefficients Λ_j described above and $\mathcal{A}_n^e$ described below. Also note that although they both relate Bessel functions of argument kr, Equations S36–S39 differ substantially from Equations S21–S24.

Following the approach of Styczinski et al. (*in progress*), we now define a final recursion quantity, the complex response to the excitation field $\mathcal{A}_n^e$ as

$$\mathcal{A}_n^e = \frac{\beta_n + \Lambda_N \gamma_n}{\delta_n + \Lambda_N \varepsilon_n} \tag{S40}$$

This normalized, complex amplitude has the desirable characteristic that it is asymptotic to $(1+0i)$ for a highly conducting ocean with no ice shell, for any degree n in the excitation field. Therefore, with the recursion relation from Equation S26, $\mathcal{A}_n^e$ is a readily calculable measure of the effectiveness of a body at behaving as a perfect conductor, and can easily be compared to spacecraft data fit to induced magnetic moments of any order n.

For the special case of a single, uniform conducting layer representing a saline ocean, the complex response evaluates to

$$\mathcal{A}_n^e = \frac{j_{n+1}(ka)y_{n+1}(ks) - j_{n+1}(ks)y_{n+1}(ka)}{j_{n+1}(ks)y_{n-1}(ka) - j_{n-1}(ka)y_{n+1}(ks)} \tag{S41}$$

with a the radius of the ocean outer boundary, s the radius of the ocean inner boundary, and $k = \sqrt{i\omega\mu_0\sigma}$ with σ the conductivity of the ocean layer. $a = R - h$, where h is the ice shell thickness, and $s = a - D$, where D is the ocean thickness. This result is analogous to the three-layer model of Zimmer et al. (2000). All past studies have considered a uniform excitation field, with $n = 1$; comparison with past work is made by evaluating $A = |\mathcal{A}_1^e|$ and $\phi = -\arg(\mathcal{A}_1^e)$.

Text S1.2 Numerical approximation to external boundary conditions

We now detail our alternative numerical approach, based on that of Eckhardt (1963). Returning to Equation S11 (the Bessel equation), if instead of solving for the basis functions directly, we make the substitution

$$\frac{dF(r)}{dr} = F(r)G(r) \tag{S42}$$

where $G(r)$ is another arbitrary function of r, we obtain a Riccati equation for G:

$$\frac{d}{dr}\Big(r^2 G\Big) + r^2 G^2 + k^2 r^2 - n(n+1) = 0 \tag{S43}$$

Note that we have not made any assumptions about $k(r)$ in reaching Equation S43.

We can now exploit the external boundary conditions to obtain a new equation. In Equations S32 and S33, on the right-hand side we insert the more general expressions from Equations S8–S10 using the above substitution for $F(r)$. Solving for the Q response as in Equation S34, we obtain

$$Q = \frac{n}{n+1}\,\frac{rG - n}{rG + n + 1} \tag{S44}$$

Taking dQ/dr and making substitutions from Equation S43, we reach an ODE for Q that may be solved numerically:

$$\frac{dQ}{dr} = -\frac{k^2 r(n+1)}{(2n+1)n}\left(Q - \frac{n}{n+1}\right)^2 - \frac{2n+1}{r}Q \tag{S45}$$

$\mathcal{A}_n^e$ may then be found by

$$\mathcal{A}_n^e = \frac{n+1}{n}Q \tag{S46}$$

as can be seen from comparing Equations S35 and S40.

Text S1.3 Application of induced response functions

As applied to the Galilean moons, the primary case of interest in the magnetic induction problem is for an imposed field that is effectively uniform, where $n = 1$. The analysis

contained in this work makes the approximation that the magnetic field applied to the Galilean moons is entirely spatially uniform, with $n = 1$. The higher-order components applied to the moons are small, mostly deriving from oscillations in the plasma at much higher frequencies than Jupiter's primary field (Schilling et al., 2007). In this case, expressing the complex quantity $\mathcal{A}_1^e$ in terms of a magnitude A and phase delay ϕ permits a direct comparison to work by other authors (e.g., Zimmer et al., 2000):

$$\mathcal{A}_1^e = Ae^{-i\phi} \tag{S47}$$

The negative exponent in Equation S47 is ultimately the result of an error in Parkinson (1983) propagated in the many past studies applying the results from that text. Our choice of sign convention for k as the complex conjugate of that chosen by Parkinson (1983), a necessary condition for deriving the spherical Bessel equation, causes our result for the complex amplitude $\mathcal{A}_1^e$ to be equal to the complex conjugate of the analogous quantity from Zimmer et al. (2000), $Ae^{i\phi}$. This merely negates the phase of this quantity, as A and ϕ are both real-valued. By defining A and ϕ as in Equation S47, we can use them exactly as in past work to evaluate the internally generated, induced magnetic field outside the moon $\mathbf{B}_{\text{int,moon}}$ by

$$\mathbf{B}_{\text{int,moon}} = -Ae^{-i(\omega t-\phi)}\,\frac{B_e}{2}\,\frac{3\cos\theta\hat{r} - \hat{z}}{r^3} \tag{S48}$$

where $\hat{z}$ is directed along the instantaneous vector of the time-varying external magnetic field $\mathbf{B}_{\text{ext,moon}}$ applied to the moon, θ is the angle between $\hat{z}$ and the measurement point at $\mathbf{r} = r\hat{r}$, the origin is centered on the body to which the excitation field is applied, and the factor of 2 in Equation S48 results from inserting $n = 1$ into the factor $n/(n+1)$ in Equation S35. Note that Equation S48 only applies in the space outside the moon.

Figures 2–4, 6, and 7 in the main text were produced using the Eckhardt (1963)-based numerical technique. Figure 6 plots $A = |\mathcal{A}_1^e|$ and $\phi = -\arg(\mathcal{A}_1^e)$ for Europa, Ganymede, and Callisto. Figures 2–4 plot the same phase delay ϕ, but scale the amplitude A to the maximum induced magnetic field that would be measured at a surface point. This occurs where the time-varying external field from Jupiter is instantaneously directed vertically into or out of the surface ($\theta = 0$ or π, $r = R$, and $\hat{r} = \pm\hat{z}$ in Equation S48). These conditions happen at key locations on the bodies' surfaces twice per period (once outward, once inward), and are not in general collocated for the various excitation frequencies. For example, for Europa's synodic period with Jupiter at 11.23 hr, the key points on the surface are the sub- and anti-jovian points, because the maximum oscillation is along the europacentric (E$\phi\Omega$) $\hat{y}$ direction. In contrast, at Europa's orbital period of 85.23 hr, the greatest oscillation is aligned with the E$\phi\Omega$ $\hat{z}$ direction, so the largest induced field will occur at the north and south spin poles. However, all of Figures 2–4, 7 scale to the B_y oscillation for ease of interpretation, and therefore describe the oscillation along the vertical at the surface at the sub- and anti-jovian points for each body.

Figures S1 and S2 show a benchmarking calculation comparing the ODE approach to the stacked layer approach. For sufficiently stringent numerical solution parameters, the two approaches yield effectively identical results. Furthermore, the ODE approach has a distinct advantage in computation time for our implementation. The stacked layer approach requires explicit calculation of many Bessel functions for the layer coefficients at closely spaced points. The results of these functions very nearly cancel, so they must be evaluated at enormously high precision. Sometimes over 200 digits of precision are

required to evaluate interior models relevant to the Galilean moons, requiring special computation packages and ample computation time.

The ODE approach, in contrast, converges faster for more closely spaced layers, which create a smoother function to evaluate. Thus, in practice we evaluate a comparable result that takes a small fraction of the time to compute for a highly detailed interior structure model. Use of the ODE approach to reduce computation time for detailed interior models enables massively parallel statistical studies, such as Monte Carlo methods, to explore large parameter spaces in reasonable time scales. In future work, we intend to apply such methods to better constrain the interior structures of the Galilean moons and other moons, with current and future measurements.

Text S1.6 Comparison of adiabatic ocean profiles to uniformly conducting oceans

In Section 2 of this work (main text), we focus on the observable signal from depth-dependent effects that shift the conductivity away from a nominal mean value. All past work studying magnetic induction of satellite oceans has assumed the ocean to be a single layer of uniform conductivity and calculated the induced field using the approach of Srivastava (1966). For comparison to this body of literature, we plot the difference in induced field from our approach to the uniform conductivity approach in Figures S3–S5. In each of these figures, the top panels compare our adiabatic ocean approach to a uniform conductivity that is consistent with the mean value from the corresponding adiabatic profile; the bottom panels compare our approach against a uniform conductivity taken to be the value from our model at the uppermost ice–ocean boundary. In most cases, the differences are near a few percent for the longer periods considered (red lines).

Text S2. Motional Induction Response Model

The magnetic induction equation can be used to estimate the components of the magnetic field $\mathbf{B}$ induced by ocean currents with velocity $\mathbf{u}$ and those arising from changes in the externally imposed field:

$$\frac{\partial \mathbf{B}}{\partial t} = \nabla \times (\mathbf{u} \times \mathbf{B}) - \nabla \times (\eta \nabla \times \mathbf{B}) \tag{S49}$$

where $\eta = (\mu_0 \sigma)^{-1}$ is the magnetic diffusivity. Here, the first term represents the evolution of the magnetic field, the second term represents magnetic induction, and the third term represents magnetic diffusion.

Neglecting variations in oceanic electrical conductivity with depth and assuming an incompressible fluid, Equation S49 simplifies to

$$\frac{\partial \mathbf{B}}{\partial t} = (\mathbf{B} \cdot \nabla)\mathbf{u} - (\mathbf{u} \cdot \nabla)\mathbf{B} + \eta \nabla^2 \mathbf{B}, \tag{S50}$$

after also expanding the induction term and utilizing $\nabla \cdot \mathbf{B} = 0$ and $\nabla \cdot \mathbf{u} = 0$. Let us decompose the total magnetic field into the background imposed field $\mathbf{B}_o$ and the satellite's induced field $\mathbf{b}$:

$$\mathbf{B} = \mathbf{B}_o + \mathbf{b} \tag{S51}$$

with $|\mathbf{B}_o| \gg |\mathbf{b}|$. The induction equation then becomes

$$\frac{\partial \mathbf{b}}{\partial t} = -\frac{\partial \mathbf{B}_o}{\partial t} + (\mathbf{B}_o \cdot \nabla)\mathbf{u} - (\mathbf{u} \cdot \nabla)(\mathbf{B}_o + \mathbf{b}) + \eta \nabla^2 (\mathbf{B}_o + \mathbf{b}) \tag{S52}$$

Here, the first term is the evolution of the induced magnetic field, the second term is induction due to variations in Jupiter's (or Ganymede's) intrinsic magnetic field, the third term is induction due to oceanic fluid motions, the fourth and fifth terms are advection of the fields by ocean flows, and the sixth and seventh terms are diffusion of the jovian and induced fields.

Let us next assume that the background field can be approximated by $\mathbf{B}_o = B_o\hat{z}$, where B_o is constant and homogeneous and $\hat{z}$ is aligned with the rotation axis, in which case Equation S52 further simplifies to:

$$\frac{\partial \mathbf{b}}{\partial t} = B_o \frac{\partial \mathbf{u}}{\partial z} - (\mathbf{u}\cdot\nabla)\mathbf{b} + \eta\nabla^2\mathbf{b}. \tag{S53}$$

We will also focus on the quasi-steady induction signal generated by ocean flows rather than the rapidly varying contribution that could be difficult to distinguish from other magnetic field perturbations. Towards this end, the induced magnetic field and velocity fields are decomposed into mean and fluctuating components: $\mathbf{b} = \overline{\mathbf{b}} + \mathbf{b}'$ and $\mathbf{u} = \overline{\mathbf{u}} + \mathbf{u}'$. Inserting this into Equation S53 and using Reynolds averaging yields

$$\frac{\partial \overline{\mathbf{b}}}{\partial t} = B_o \frac{\partial \overline{\mathbf{u}}}{\partial z} - (\overline{\mathbf{u}}\cdot\nabla)\overline{\mathbf{b}} - \overline{(\mathbf{u}'\cdot\nabla)\mathbf{b}'} + \eta\nabla^2\overline{\mathbf{b}}. \tag{S54}$$

Next, we focus on the radial and latitudinal components because the zonal flow ($\overline{u}_\phi$) is nearly invariant in the z-direction (Figure 8a), noting also that azimuthally oriented (toroidal) magnetic fields would not be detectable by spacecraft:

$$\frac{\partial \overline{b}_r}{\partial t} = B_o \frac{\partial \overline{u}_r}{\partial z} - (\overline{\mathbf{u}}\cdot\nabla)\overline{b}_r - \overline{(\mathbf{u}'\cdot\nabla)b'_r} + \eta\nabla^2\overline{b}_r \tag{S55}$$

$$\frac{\partial \overline{b}_\theta}{\partial t} = B_o \frac{\partial \overline{u}_\theta}{\partial z} - (\overline{\mathbf{u}}\cdot\nabla)\overline{b}_\theta - \overline{(\mathbf{u}'\cdot\nabla)b'_\theta} + \eta\nabla^2\overline{b}_\theta \tag{S56}$$

Using simple scaling arguments, the second and third terms on the right sides are likely small compared to the first term since $|B_o| \gg |b|$ (assuming similar characteristic flow speeds and length scales) such that

$$\frac{\partial \overline{b}_r}{\partial t} \approx B_o \frac{\partial \overline{u}_r}{\partial z} + \eta\nabla^2\overline{b}_r \tag{S57}$$

$$\frac{\partial \overline{b}_\theta}{\partial t} \approx B_o \frac{\partial \overline{u}_\theta}{\partial z} + \eta\nabla^2\overline{b}_\theta. \tag{S58}$$

Considering the poloidal flow components (Figure 8b-c), the induced fields would likely be strongest near the equator where large vertical gradients in the convective flows exist.

In the steady-state limit and approximating the gradient length scales as D and flow speeds as U_r and U_θ, an upper bound on magnetic fields induced by ocean currents can be estimated as:

$$\frac{B_o U_r}{D} \sim \frac{\eta b_r}{D^2}, \text{ such that } b_r \sim \frac{B_o U_r D}{\eta} = \mu_o \sigma D U_r B_o \tag{S59}$$

$$\frac{B_o U_\theta}{D} \sim \frac{\eta b_\theta}{D^2}, \text{ such that } b_\theta \sim \frac{B_o U_\theta D}{\eta} = \mu_o \sigma D U_\theta B_o. \tag{S60}$$

Here, we neglect the coupling between b_r and b_θ to effectively estimate maximum values for each component.

Several aspects regarding the velocity field should also be mentioned. First, the oceans are assumed to be in a convective regime that is weakly constrained by rotation following Soderlund (2019). Soderlund19 also notes, however, that a stronger rotational influence may be possible, which would lead to slower flow speeds and weaker induced magnetic fields. In addition, it is possible that the models overestimate the meridional circulations relative to the zonal flows compared to what might be expected in the satellites (e.g., Jones & Kuzanyan, 2009). Because our approach focuses on upper bound estimates, the results are still valid if meridional circulations within the oceans are weaker than those modeled. Finally, flows due to libration, precession, tides, and electromagnetic pumping (e.g., Le Bars et al., 2015; Gissinger & Petitdemange, 2019; Soderlund et al., 2020) are neglected here but may interact with the convective flows to change their configurations and/or speeds.

Text S3. Interior Structure Models

The interior structures and associated electrical conductivities used in this work are computed with the PlanetProfile package described by Vance et al. (2018). PlanetProfile employs self-consistent thermodynamics for the properties of ice, fluids, rock, and metals to compute the radial structure of an ocean world. Inputs are the surface temperature and bottom melting temperature of the ice, T_o and T_b; density of the rocky interior and any metallic core, ρ_{mantle} and ρ_{core}; salinity of the ocean, w; and gravitational moment of inertia, C/MR^2. For this work, the values for these properties are substantially the same as those used by Vance et al. (2018), with a few minor changes that do not significantly change the ocean thickness and electrical conductivity that are central to this work.

Properties of ice are now computed using the SeaFreeze package (Journaux et al., 2020), which provides substantial improvements in accuracy for conditions relevant to icy moon interiors. Solid-state convection in the surface ice I layer has been corrected from Vance et al. (2018) to use the thermal upper boundary layer thickness, e_{th}, from Deschamps and Sotin (2001) rather than the mechanical thickness, e_{mech}. Properties of the rocky mantle and metallic core for Europa are based on updated mineralogies described by Vance and Melwani Daswani (2020). The silicate mantle composition is that of the *MC-Scale* model, an aggregate of type CM and CI chondrite compositions, and the composition of comet 67P. The core composition is a Fe–FeS mixture containing 5 wt% sulfur. Sulfur is appropriately partitioned between the mantle and core to preserve bulk planetary distribution of sulfur in the *MC-Scale* model. This approach does not account for the addition of sulfur to the ocean, which makes up 2.6% of the ocean's mass for the 10 wt% $MgSO_4$ case.

The effect of this minor inconsistency on the thickness of the ocean is smaller than the few-km variation in ocean thicknesses between the different ocean compositions (Table 1).

Using the moment of inertia along with supposed core and mantle densities to inform the construction of interior models effectively fixes the hydrosphere thickness. For example, for Europa we use the mean value from Anderson et al. (1998) of $C/MR^2 = 0.346 \pm 0.005$. The error bars in this result, combined with the assumed densities of the different radial layers, provide the canonical range of hydrosphere thicknesses of 80–170 km. Our choice of the fixed value of 0.346, and the fixed core and mantle density, create the ocean+ice hydrosphere thickness of about 125 km. This applies to all interior structures considered for this body. The near-fixed hydrosphere thicknesses are evident in the positions of the filled circles in Figure 5. Note that the interior structures we infer from moments of inertia restrict the realistic parameter space in Figures 2–4 to be a narrow region near the top of each contour plot. This is demonstrated in Figures S8–S10, wherein the studied models are marked on the contours from Figures 2–4.

The discrete layers in PlanetProfile are in sufficient number to provide step transitions between layers that are smaller than 1 km in the hydrospheres and smaller than a few km in the deeper interior. For example, the Europa models used here employ 200 steps in the ice, 350 steps in the ocean, 500 steps in the silicate layer, and 10 steps in the core. Similar scalings are used for Ganymede and Callisto in proportion to their thicker oceans and ice layers.

References

Anderson, J., Schubert, G., Jacobson, R., Lau, E., Moore, W., & Sjogren, W. (1998). Europa's differentiated internal structure: inferences from four Galileo encounters.

Science, *281*(5385), 2019 - 2022.

Deschamps, F., & Sotin, C. (2001). Thermal convection in the outer shell of large icy satellites. *Journal of Geophysical Research: Planets*, *106*(E3), 5107–5121. doi: 10.1029/2000je001253

Eckhardt, D. H. (1963). Geomagnetic induction in a concentrically stratified earth. *Journal of Geophysical Research*, *68*(23), 6273–6278. doi: 10.1029/jz068i023p06273

Gissinger, C., & Petitdemange, L. (2019). A magnetically driven equatorial jet in Europa's ocean. *Nature Astron.*, *1*.

Hartkorn, O., & Saur, J. (2017). Induction signals from Callisto's ionosphere and their implications on a possible subsurface ocean. *Journal of Geophysical Research: Space Physics*, *122*(11), 11,677–11,697. doi: 10.1002/2017ja024269

Jones, C. A., & Kuzanyan, K. M. (2009). Compressible convection in the deep atmospheres of giant planets. *Icarus*, *358*, 873–897.

Journaux, B., Brown, J., Pakhomova, A., Collings, I., Petitgirard, S., Espinoza, P., ... et al. (2020). Holistic approach for studying planetary hydrospheres: Gibbs representation of ices thermodynamics, elasticity and the water phase diagram to 2300 MPa. *Journal of Geophysical Research: Planets*, *125*, e2019JE006176. doi: 10.1029/2019je006176

Le Bars, M., Cebron, D., & Le Gal, P. (2015). Flows driven by libration, precession, and tides. *Annu. Rev. Fluid Mech.*, *47*, 163–193.

Parkinson, W. (1983). *Introduction to geomagnetism.* Scottish Academic Press (Edinburgh).

Saur, J., Neubauer, F. M., & Glassmeier, K.-H. (2009). Induced magnetic fields in solar

system bodies. *Space Science Reviews*, *152*(1-4), 391–421. doi: 10.1007/s11214-009-9581-y

Schilling, N., Neubauer, F. M., & Saur, J. (2007). Time-varying interaction of europa with the jovian magnetosphere: Constraints on the conductivity of Europa's subsurface ocean. *Icarus*, *192*(1), 41–55.

Soderlund, K. M. (2019). Ocean dynamics of outer solar system satellites. *Geophys. Res. Lett.*, https://doi.org/10.1029/2018GL081880.

Soderlund, K. M., Kalousová, K., Buffo, J. J., Glein, C. R., Goodman, J. C., Mitri, G., ... others (2020). Ice-ocean exchange processes in the jovian and saturnian satellites. *Space Science Reviews*, *216*(5), 1–57.

Srivastava, S. P. (1966). Theory of the magnetotelluric method for a spherical conductor. *Geophysical Journal International*, *11*(4), 373–387. doi: 10.1111/j.1365-246x.1966.tb03090.x

Vance, S. D., & Melwani Daswani, M. (2020). Serpentinite and the search for life beyond Earth. *Phil. Trans. R. Soc. A*, *378*(2165), 20180421.

Vance, S. D., Panning, M. P., Stähler, S., Cammarano, F., Bills, B. G., Tobie, G., ... et al. (2018). Geophysical investigations of habitability in ice-covered ocean worlds. *Journal of Geophysical Research: Planets*. doi: 10.1002/2017je005341

Zimmer, C., Khurana, K. K., & Kivelson, M. G. (2000). Subsurface oceans on Europa and Callisto: Constraints from Galileo magnetometer observations. *Icarus*, *147*(2), 329–347.

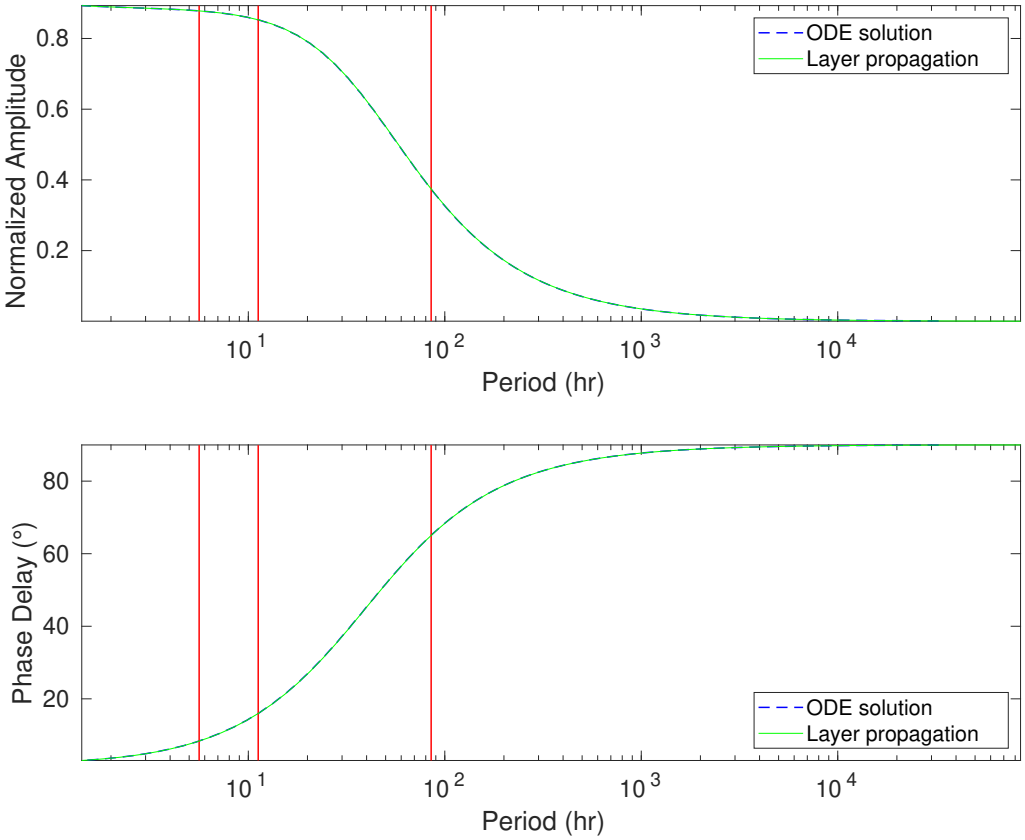

Figure S1. Comparison of the complex response $\mathcal{A}_1^e$ for the uniform field case, calculated by two different methods. The amplitude $A = |\mathcal{A}_1^e|$ and phase delay $\phi = -\arg(\mathcal{A}_1^e)$ are plotted separately. The Srivastava (1966) layered conductor approach common in the literature is plotted as a blue dashed line and the Eckhardt (1963) ODE approach we use in our analysis is plotted in as a solid green line. For sufficiently stringent numerical solution parameters, the lines are effectively identical. A numerically challenging example case was selected for this comparison: a Europa model of approx. 150 layers and a 1 wt% $MgSO_4$ ocean.

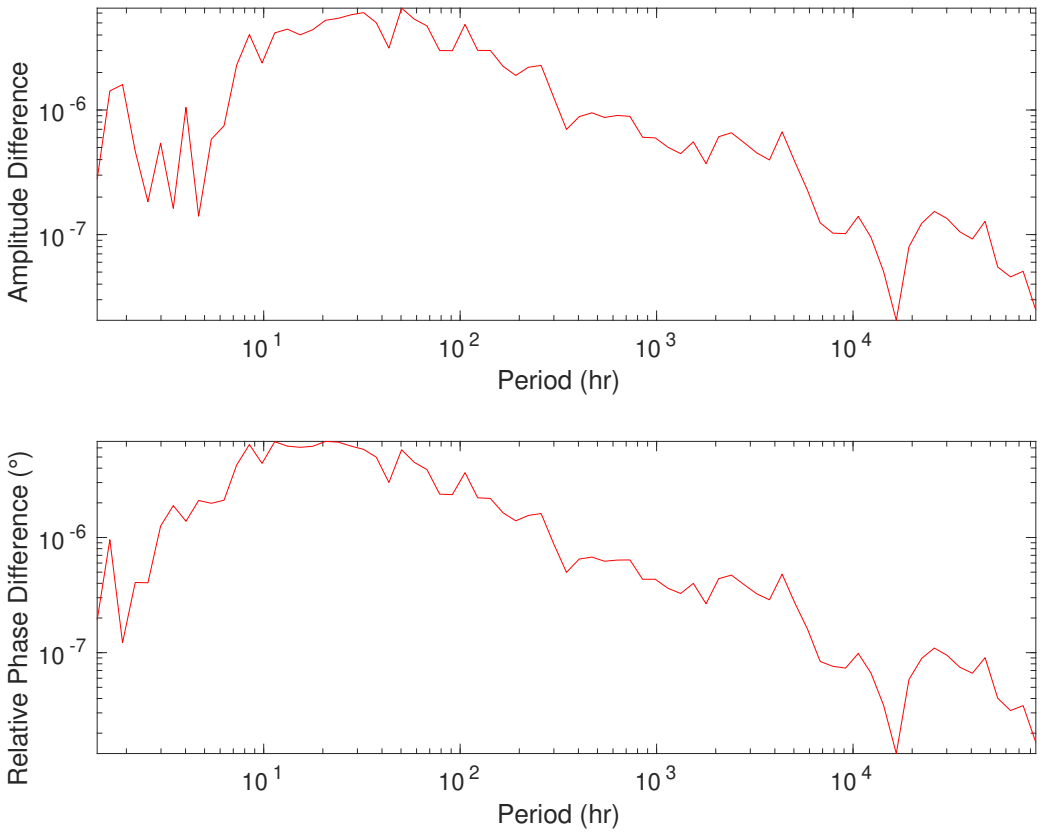

Figure S2. Difference of the lines in Figure S1. Absolute values of the difference are plotted so that a log scale may be used to display them. The relative phase difference is shown, i.e. normalized to a maximum of 1. The small differences belie the close overlap of the lines in Figure S1.

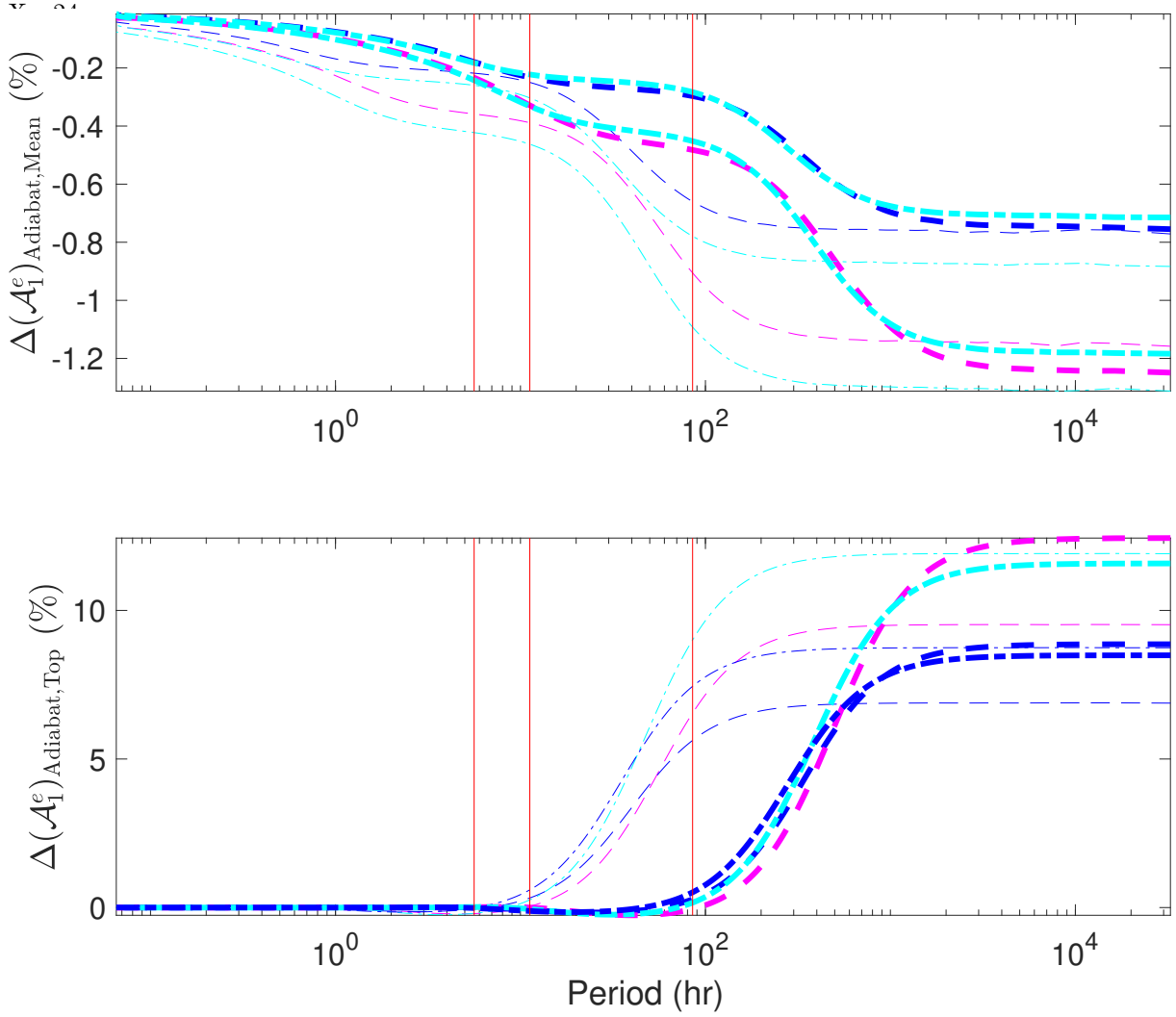

Figure S3. Europa: Differences (in %) from the nominal adiabatic case studied here, for uniformly conducting oceans with the equivalent mean conductivity (top panel), and for uniformly conducting oceans with the equivalent conductivity at the ice–ocean interface (bottom panel). Dashed lines (−−) are $MgSO_4$ oceans; dot–dashed lines are seawater oceans (-·-). Blue curves are for thicker ice (30 km), magenta curves are thinner ice (5 km) $MgSO_4$ oceans, and cyan curves are thinner ice (5 km) seawater oceans. Thick lines are higher salinities (10 wt% and 3.5 Wt%, respectively) for oceans with aqueous $MgSO_4$ and seawater. Thinner lines are for oceans with 10% of those concentrations. Vertical lines are the strongest inducing frequencies shown in Figure 1.

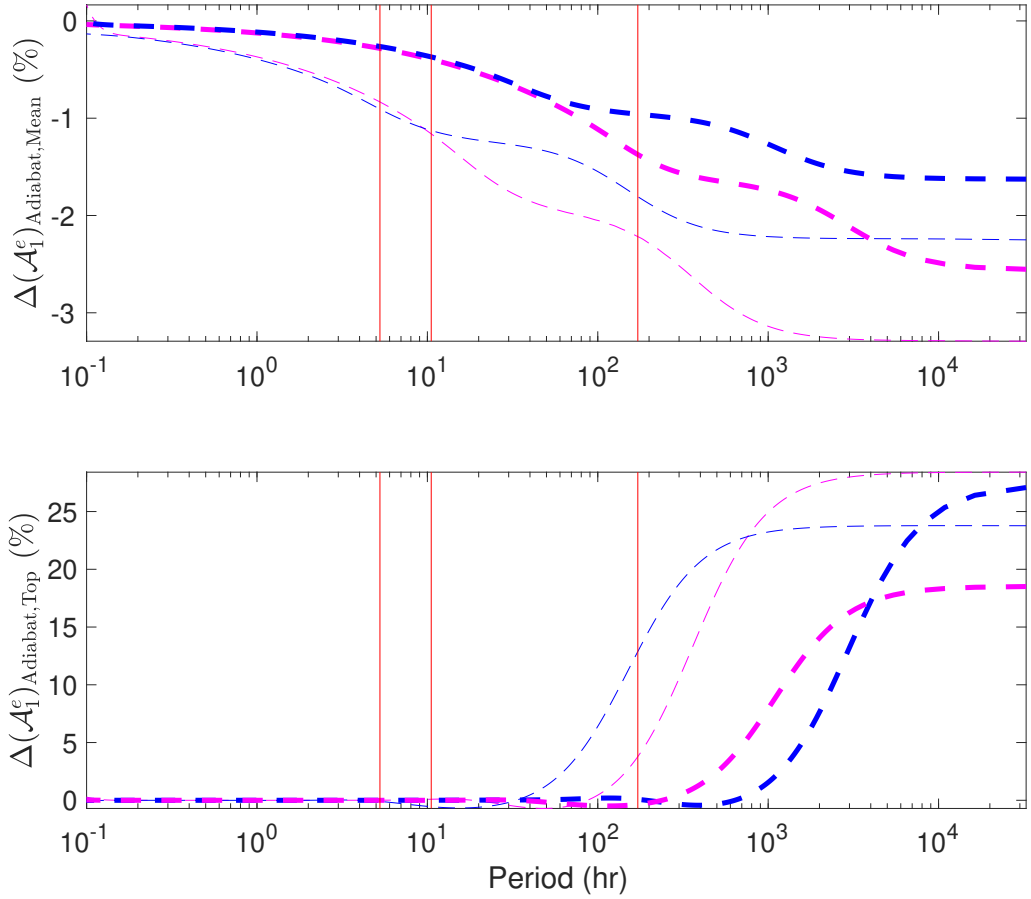

Figure S4. Ganymede: Differences (in %) from the nominal adiabatic case studied here for uniformly conducting oceans with the equivalent mean conductivity (top panel), and for uniformly conducting oceans with the equivalent conductivity at the ice–ocean interface (bottom panel). Magenta curves are for thinner ice (∼30 km) and blue curves are for thicker ice (∼100 km). All configurations assume an ocean with aqueous $MgSO_4$. Thick lines are higher salinity (10 wt%) and thinner lines are for oceans with 1 wt%. Vertical lines are the strongest inducing frequencies shown in Figure 1.

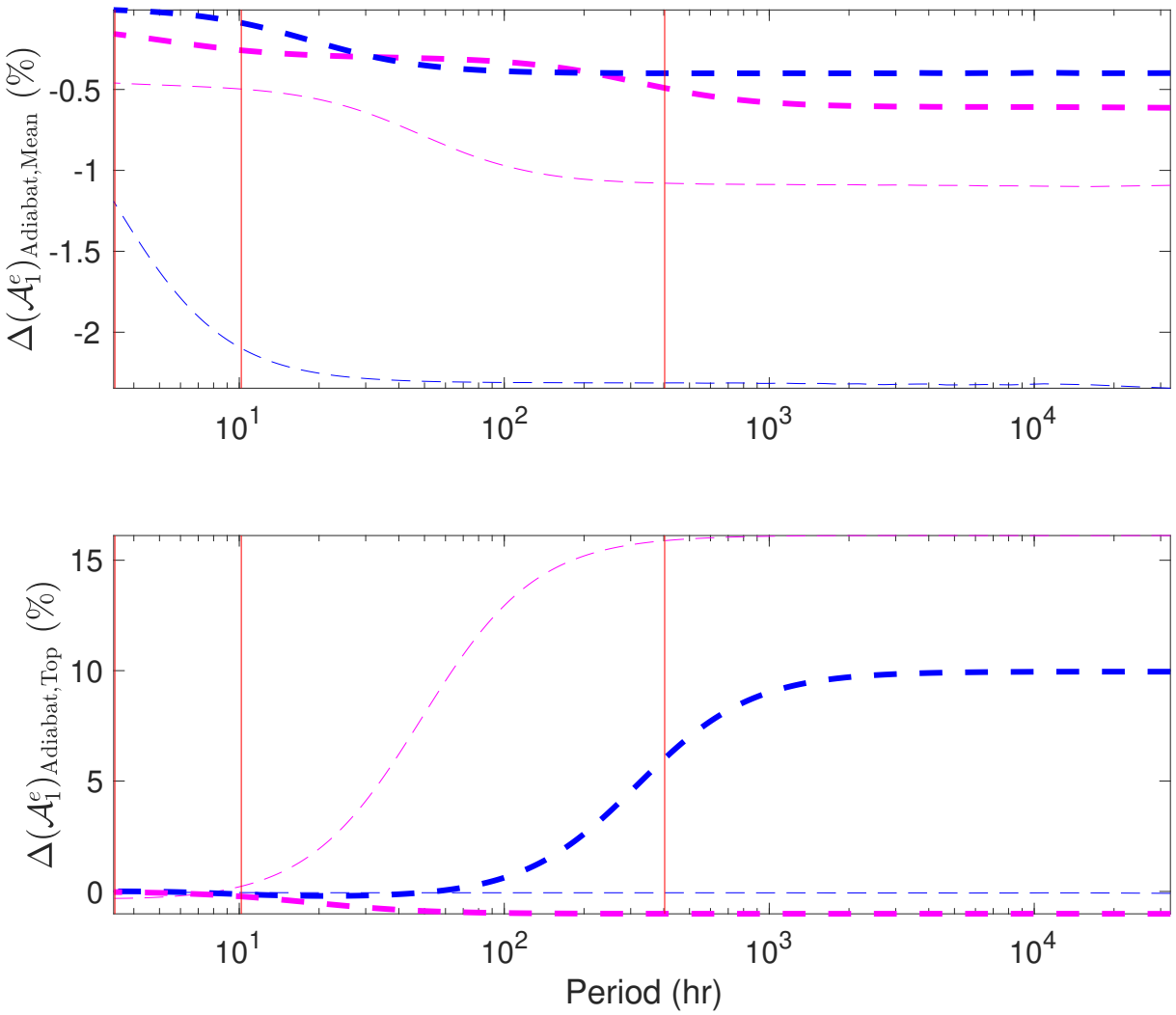

Figure S5. Callisto: Differences (in %) from the nominal adiabatic case studied here, for uniformly conducting oceans with the equivalent mean conductivity (top panel) and with for uniformly conducting oceans with the equivalent conductivity at the ice–ocean interface (bottom panel). Magenta curves are for thinner ice (∼30 km) and blue curves are for thicker ice (∼100 km). All configurations assume an ocean with aqueous $MgSO_4$. Thick lines are higher salinity (10 wt%) and thinner lines are for oceans with 1 wt%. Vertical lines are the strongest inducing frequencies shown in Figure 1.

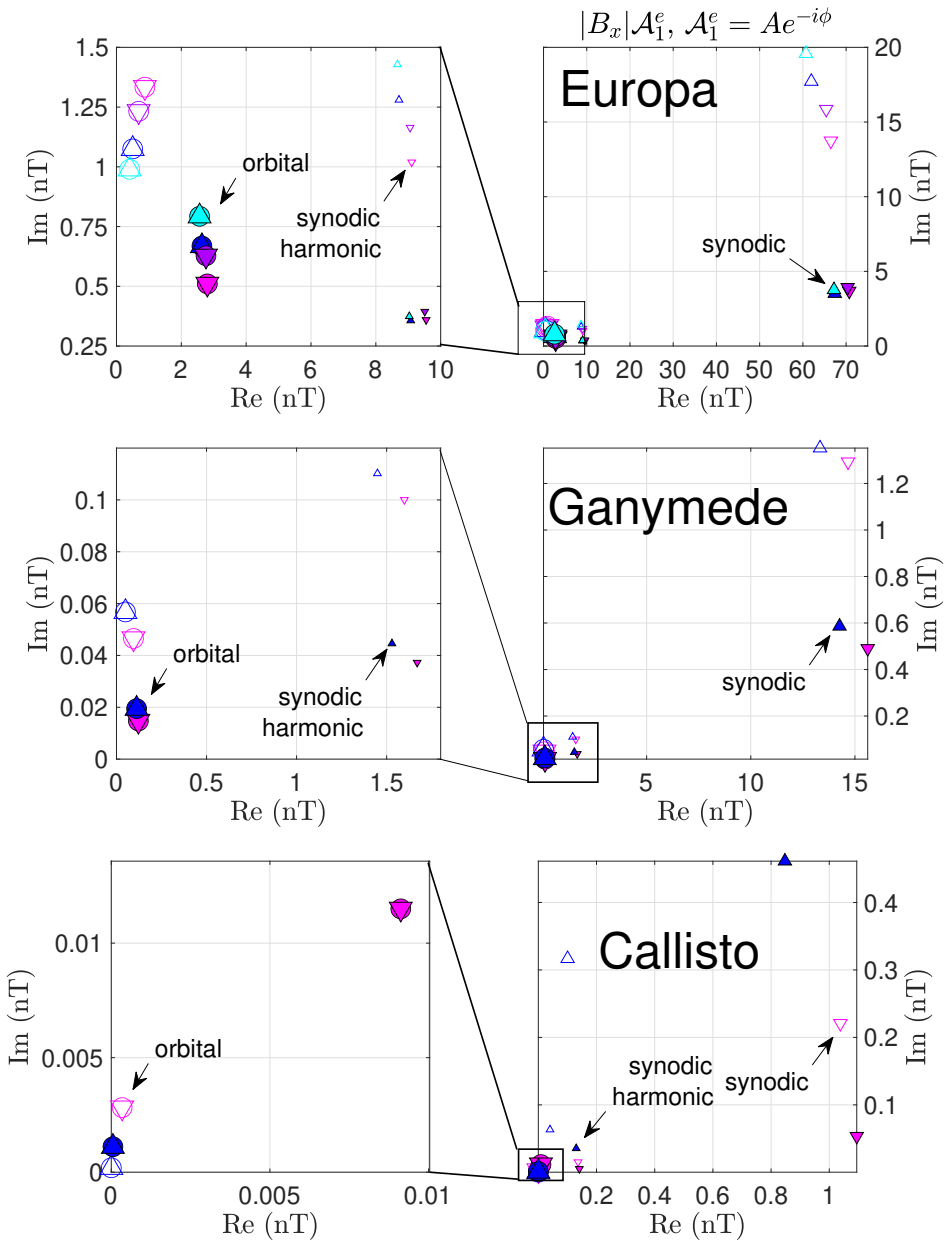

Figure S6. Real and imaginary components of the diffusive induction response to the changing B_x component of Jupiter's magnetic field at the main driving periods (Figure 1) for {Europa,Ganymede,Callisto}. The real part (on the x-axis) is in phase with the excitation field, and the imaginary part (on the y-axis) is 90° out of phase, as detailed in Section 2.6. Subpanels on the left side show the lower-magnitude signals of panels on the right. Filled symbols are for the higher concentrations. Upward and downward triangles are for thicker ice ({30,95,130} km) and thinner ice ({5,26,100} km), respectively. Symbol sizes scale with the period of the oscillation, denoting the orbital (largest), the synodic (intermediate), and the synodic harmonic (smallest). Circles are added to the orbital periods to guide the eye.

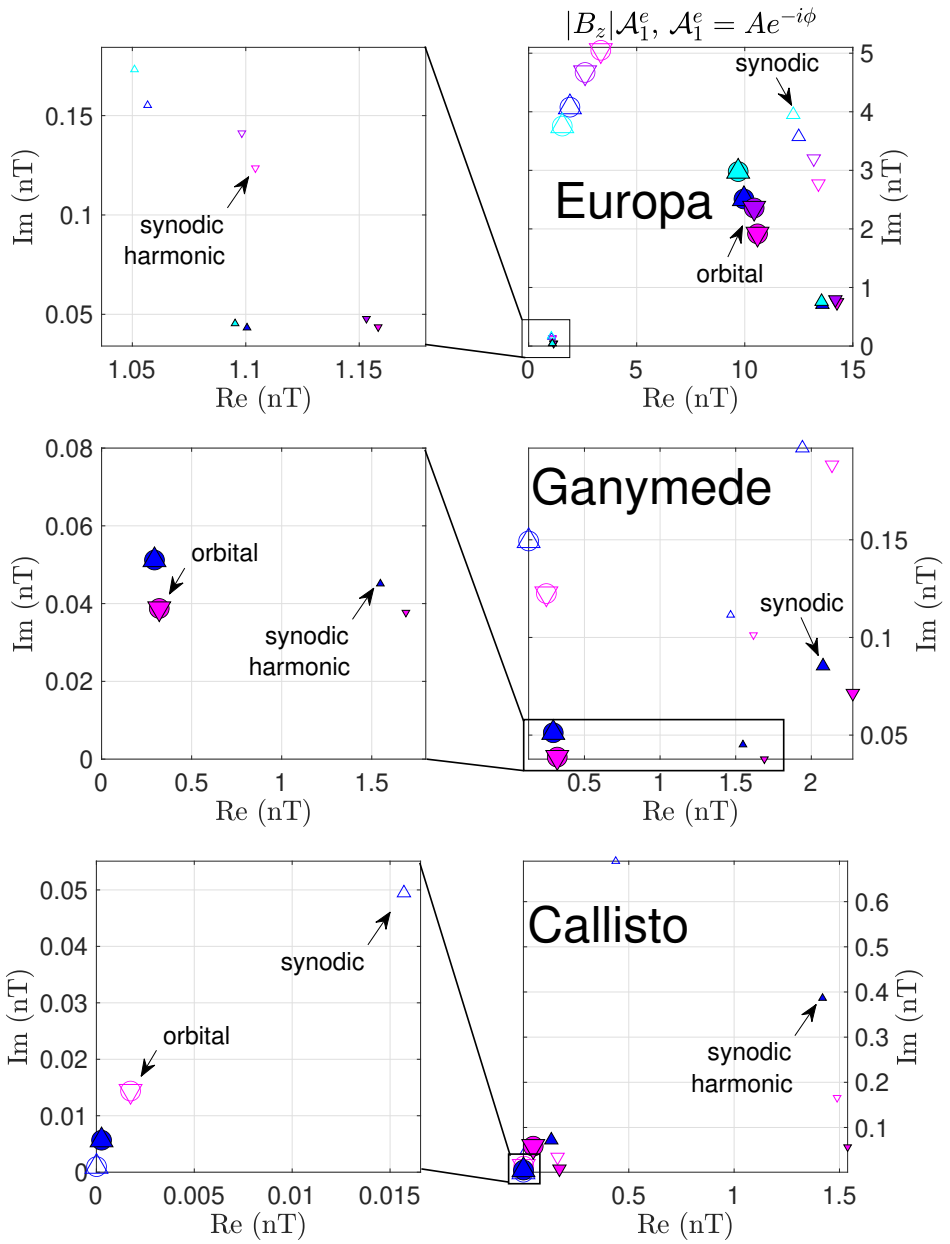

Figure S7. Real and imaginary components of the diffusive induction responses to the changing B_z component of Jupiter's magnetic field at the main driving periods (Figure 1) for {Europa,Ganymede,Callisto}. The real part (on the x-axis) is in phase with the excitation field, and the imaginary part (on the y-axis) is 90° out of phase, as detailed in Section 2.6. Subpanels on the left side show the lower-magnitude signals of panels on the right. Filled symbols are for the higher concentrations. Upward and downward triangles are for thicker ice ({30,95,130} km) and thinner ice ({5,26,100} km), respectively. Symbol sizes scale with the period of the oscillation, denoting the orbital (largest), the synodic (intermediate), and the synodic harmonic (smallest). Circles are added to the orbital periods to guide the eye.

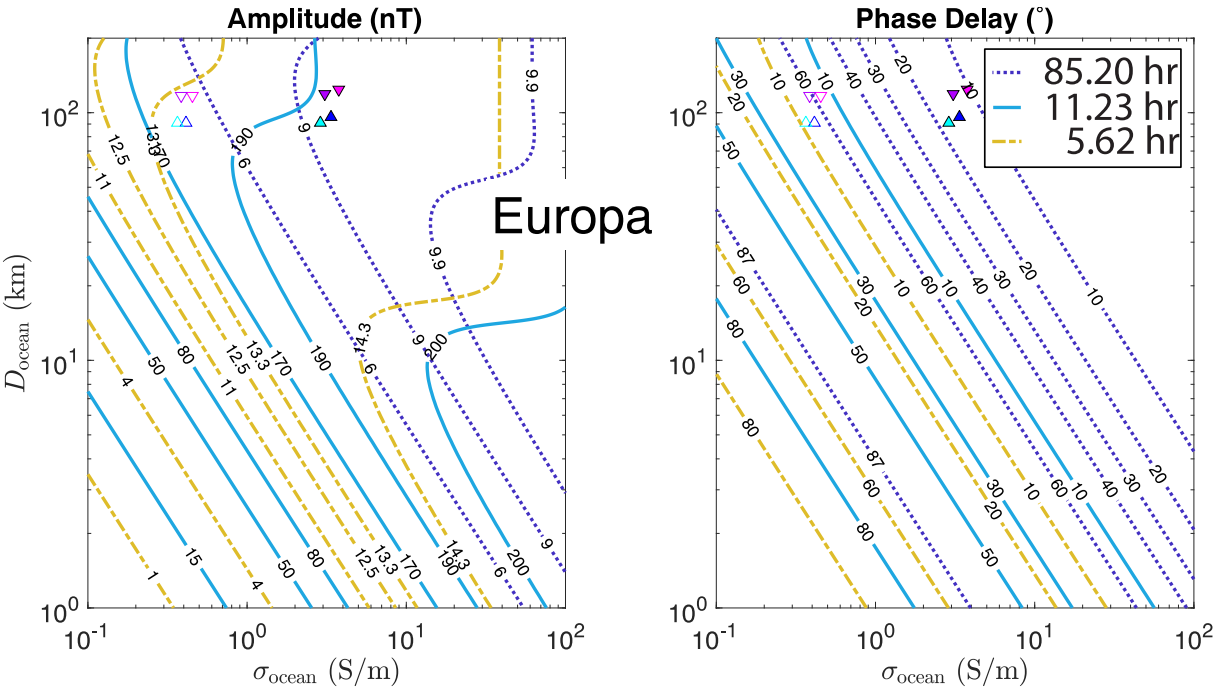

Figure S8. Europa: Reproduction of main text Figure 2, with points showing the coordinates of the studied models. The marked points match the identification scheme described in Figure 7.

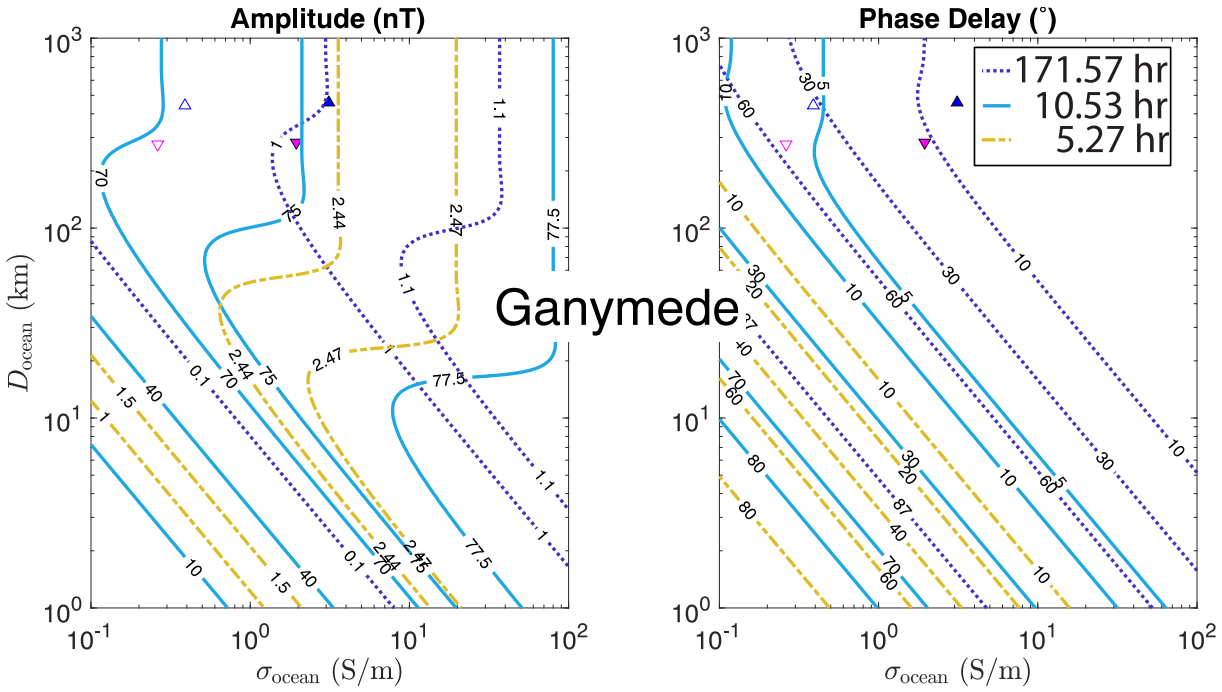

Figure S9. Ganymede: Reproduction of main text Figure 3, with points showing the coordinates of the studied models. The marked points match the identification scheme described in Figure 7.

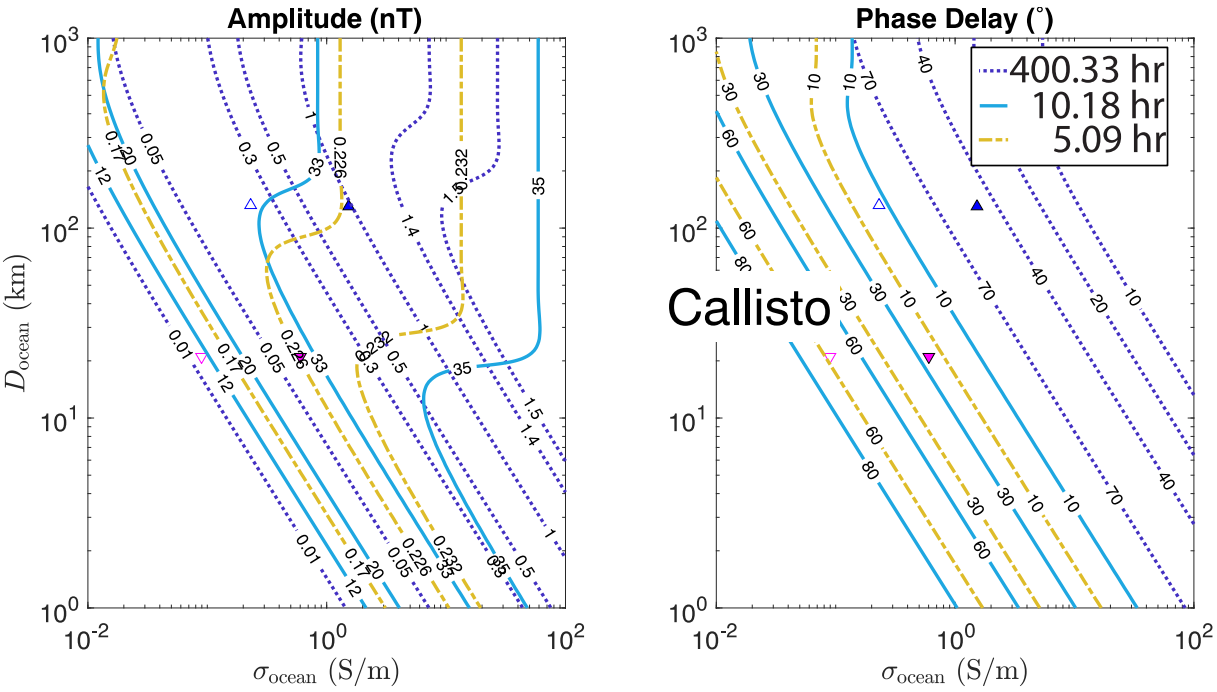

Figure S10. Callisto: Reproduction of main text Figure 4, with points showing the coordinates of the studied models. The marked points match the identification scheme described in Figure 7.

Europa			Period (hr):	**5.62**	**11.23**	**85.20**
			B_x (nT):	**10.03**	**75.55**	**3.17**
T_b (K)	$\overline{T}$ (K)	$D_{\rm I}$ (km)	$D_{\rm ocean}$ (km)		$B_x\mathcal{A}_1^e$ (nT)	
Ionosphere Only				**Re Im**	**Re Im**	**Re Im**
Pedersen				0.000 0.069	0.001 0.262	0.000 0.001
$MgSO_4$ 1 wt%				**Re Im**	**Re Im**	**Re Im**
273.1	273.9	5	117	9.106 1.019	66.471 13.737	0.876 1.333
Pedersen				9.108 1.021	66.488 13.741	0.877 1.334
$\overline{\sigma}$ = 0.4533 S/m		$\Delta\mathcal{A}_1^e$ (%)		0.36 -0.41	0.39 -0.08	0.85 0.50
$\sigma_{\rm top}$ = 0.4107 S/m		$\Delta\mathcal{A}_1^e$ (%)		0.10 7.75	-0.45 8.80	-12.31 -3.57
270.4	271.1	30	91	8.714 1.280	61.952 17.717	0.500 1.075
Pedersen				8.718 1.282	61.980 17.723	0.501 1.076
$\overline{\sigma}$ = 0.4132 S/m		$\Delta\mathcal{A}_1^e$ (%)		0.22 -0.10	0.24 0.01	0.55 0.34
$\sigma_{\rm top}$ = 0.3847 S/m		$\Delta\mathcal{A}_1^e$ (%)		-0.09 6.49	-0.88 6.09	-10.65 -4.23
$MgSO_4$ 10 wt%				**Re Im**	**Re Im**	**Re Im**
272.7	274.1	5	124	9.552 0.359	70.730 3.681	2.803 0.510
Pedersen				9.553 0.361	70.733 3.687	2.803 0.510
$\overline{\sigma}$ = 3.7646 S/m		$\Delta\mathcal{A}_1^e$ (%)		0.23 -3.83	0.33 -2.87	0.49 -0.10
$\sigma_{\rm top}$ = 3.3197 S/m		$\Delta\mathcal{A}_1^e$ (%)		-0.01 2.28	-0.01 2.13	-0.34 11.33
269.8	270.8	30	96	9.075 0.357	67.382 3.517	2.635 0.668
Pedersen				9.076 0.359	67.386 3.526	2.636 0.669
$\overline{\sigma}$ = 3.3661 S/m		$\Delta\mathcal{A}_1^e$ (%)		0.18 -2.30	0.23 -1.35	0.30 0.02
$\sigma_{\rm top}$ = 3.0763 S/m		$\Delta\mathcal{A}_1^e$ (%)		-0.01 1.41	0.08 2.77	-0.81 7.99
Seawater 0.35165 wt%				**Re Im**	**Re Im**	**Re Im**
274.9	275.7	5	117	9.076 1.102	65.860 14.958	0.758 1.275
Pedersen				9.078 1.103	65.879 14.961	0.759 1.276
$\overline{\sigma}$ = 0.4124 S/m		$\Delta\mathcal{A}_1^e$ (%)		0.41 -0.33	0.44 -0.04	0.96 0.58
$\sigma_{\rm top}$ = 0.3670 S/m		$\Delta\mathcal{A}_1^e$ (%)		0.05 9.74	-0.77 10.45	-15.30 -5.17
270.0	270.7	30	91	8.667 1.428	60.705 19.584	0.407 0.990
Pedersen				8.670 1.430	60.738 19.589	0.408 0.991
$\overline{\sigma}$ = 0.3651 S/m		$\Delta\mathcal{A}_1^e$ (%)		0.26 -0.07	0.29 0.03	0.65 0.42
$\sigma_{\rm top}$ = 0.3339 S/m		$\Delta\mathcal{A}_1^e$ (%)		-0.23 8.27	-1.49 7.33	-13.72 -5.87
Seawater 3.5165 wt%				**Re Im**	**Re Im**	**Re Im**
270.8	271.9	5	119	9.509 0.394	70.355 3.930	2.761 0.628
Pedersen				9.510 0.396	70.358 3.936	2.761 0.628
$\overline{\sigma}$ = 3.0760 S/m		$\Delta\mathcal{A}_1^e$ (%)		0.24 -3.32	0.33 -2.24	0.46 -0.03
$\sigma_{\rm top}$ = 2.7347 S/m		$\Delta\mathcal{A}_1^e$ (%)		-0.02 2.08	0.04 2.37	-0.74 10.53
268.2	269.1	30	91	9.032 0.374	67.196 3.767	2.564 0.793
Pedersen				9.033 0.376	67.201 3.777	2.564 0.793
$\overline{\sigma}$ = 2.8862 S/m		$\Delta\mathcal{A}_1^e$ (%)		0.18 -1.89	0.22 -0.95	0.28 0.03
$\sigma_{\rm top}$ = 2.6476 S/m		$\Delta\mathcal{A}_1^e$ (%)		0.01 1.46	0.10 3.88	-1.26 7.23

Table S1. Europa: Magnetic induction field strengths {Re,Im}($B_x\mathcal{A}_n^e$), in nT, at the main inducing periods in Figure 1. For the different ocean compositions and thicknesses of the upper ice I lithosphere/ocean ($D_{\rm I}/D_{\rm ocean}$; Figure 6), the adiabatic response is listed first. These values are also shown in Figure S6. Following these are the deviations from the adiabatic case (in %) for the responses including a 100 km ionosphere with Pedersen conductance of 30 S (Hartkorn & Saur, 2017), then for the ocean with uniform conductivity set to the mean of the adiabatic ocean ($\overline{\sigma}$), and then for the case with uniform conductivity set to the value at the ice–ocean interface ($\sigma_{\rm top}$). The surface responses of the ionosphere in the absence of an ocean are listed at the top of the table.

Ganymede			Period (hr):	**5.27**	**10.53**	**171.57**
			B_x (nT):	**1.76**	**16.64**	**0.14**
T_b (K)	$\overline{T}$ (K)	$D_{\rm I}$ (km)	$D_{\rm ocean}$ (km)		$B_x\mathcal{A}_1^e$ (nT)	
Ionosphere Only				**Re Im**	**Re Im**	**Re Im**
Pedersen				0.000 0.001	0.000 0.007	0.000 0.000
$MgSO_4$ 1 wt%				**Re Im**	**Re Im**	**Re Im**
270.7	279.0	25	442	1.598 0.100	14.669 1.293	0.094 0.047
Pedersen				1.598 0.100	14.669 1.293	0.094 0.047
$\overline{\sigma}$ = 0.5166 S/m			$\Delta\mathcal{A}_1^e$ (%)	0.87 -8.82	1.23 -7.04	2.61 1.01
$\sigma_{\rm top}$ = 0.3890 S/m			$\Delta\mathcal{A}_1^e$ (%)	-0.03 4.54	-0.14 5.86	-9.33 17.09
261.6	266.2	92	276	1.449 0.110	13.326 1.352	0.050 0.057
Pedersen				1.449 0.110	13.326 1.353	0.050 0.057
$\overline{\sigma}$ = 0.3322 S/m			$\Delta\mathcal{A}_1^e$ (%)	0.95 -5.29	1.18 -2.65	2.44 1.41
$\sigma_{\rm top}$ = 0.2623 S/m			$\Delta\mathcal{A}_1^e$ (%)	0.08 3.83	0.45 10.74	-22.82 -3.32
$MgSO_4$ 10 wt%				**Re Im**	**Re Im**	**Re Im**
270.2	278.3	25	458	1.670 0.037	15.614 0.490	0.122 0.015
Pedersen				1.670 0.037	15.614 0.491	0.122 0.015
$\overline{\sigma}$ = 4.0699 S/m			$\Delta\mathcal{A}_1^e$ (%)	0.29 -10.57	0.41 -9.78	1.48 -3.07
$\sigma_{\rm top}$ = 3.1150 S/m			$\Delta\mathcal{A}_1^e$ (%)	-0.00 2.03	-0.01 2.84	-0.18 7.55
260.0	263.5	93	282	1.530 0.045	14.262 0.586	0.112 0.019
Pedersen				1.530 0.045	14.262 0.586	0.112 0.019
$\overline{\sigma}$ = 2.3476 S/m			$\Delta\mathcal{A}_1^e$ (%)	0.27 -7.17	0.38 -6.43	1.01 -0.28
$\sigma_{\rm top}$ = 1.9483 S/m			$\Delta\mathcal{A}_1^e$ (%)	0.00 1.71	-0.00 2.51	-0.11 15.65
bottom layer: 30 km 20 S/m			$\Delta\mathcal{A}_1^e$ (%)	0.00 -0.00	0.00 -0.00	-1.20 0.20
Pedersen			$\Delta\mathcal{A}_1^e$ (%)	0.00 0.10	0.00 0.04	-1.20 0.20

Table S2. Ganymede: Magnetic induction field strengths {Re,Im}($B_x\mathcal{A}_n^e$), in nT, at the main inducing periods in Figure 1. For the different ocean compositions and thicknesses of the upper ice I lithosphere/ocean ($D_{\rm I}/D_{\rm ocean}$; Figure 6), the adiabatic response is listed first. These values are also shown in Figure S7. Following these are the deviations from the adiabatic case (in %) for the responses including a 100 km ionosphere with Pedersen conductance of 2 S (Hartkorn & Saur, 2017), then for the ocean with uniform conductivity set to the mean of the adiabatic ocean ($\overline{\sigma}$), and then for the case with uniform conductivity set to the value at the ice–ocean interface ($\sigma_{\rm top}$). The surface responses of the ionosphere in the absence of an ocean are listed at the top of the table.

Callisto			Period (hr):	**5.09**	**10.18**	**400.33**
			B_x (nT):	**0.17**	**1.31**	**0.03**
T_b (K)	$\overline{T}$ (K)	$D_{\rm I}$ (km)	$D_{\rm ocean}$ (km)		$B_x\mathcal{A}_1^e$ (nT)	
Ionosphere Only				**Re Im**	**Re Im**	**Re Im**
Pedersen				0.013 0.047	0.027 0.193	0.000 0.000
Cowling				0.154 0.065	0.832 0.701	0.000 0.001
$MgSO_4$ 1 wt%				**Re Im**	**Re Im**	**Re Im**
257.4	259.6	99	132	0.137 0.015	1.038 0.221	0.000 0.003
Pedersen				0.139 0.017	1.054 0.228	0.000 0.003
Cowling				0.154 0.024	1.159 0.250	0.001 0.004
$\overline{\sigma}$ = 0.2307 S/m			$\Delta\mathcal{A}_1^e$ (%)	0.49 -0.44	0.53 -0.08	1.45 0.96
$\sigma_{\rm top}$ = 0.1965 S/m			$\Delta\mathcal{A}_1^e$ (%)	0.06 14.62	-1.03 15.03	-26.08 -13.62
250.8	250.9	128	21	0.040 0.063	0.101 0.317	0.000 0.000
Pedersen				0.068 0.079	0.199 0.459	0.000 0.000
Cowling				0.159 0.055	0.950 0.656	0.000 0.001
$\overline{\sigma}$ = 0.0895 S/m			$\Delta\mathcal{A}_1^e$ (%)	0.04 0.02	0.04 0.03	0.05 0.03
$\sigma_{\rm top}$ = 0.0874 S/m			$\Delta\mathcal{A}_1^e$ (%)	-3.26 -0.99	-4.12 -1.87	-4.52 -2.28
$MgSO_4$ 10 wt%				**Re Im**	**Re Im**	**Re Im**
255.7	256.9	99	130	0.141 0.005	1.094 0.053	0.009 0.011
Pedersen				0.142 0.007	1.098 0.062	0.009 0.012
Cowling				0.151 0.018	1.135 0.118	0.010 0.012
$\overline{\sigma}$ = 1.5256 S/m			$\Delta\mathcal{A}_1^e$ (%)	0.20 -2.91	0.26 -1.74	0.69 0.39
$\sigma_{\rm top}$ = 1.3789 S/m			$\Delta\mathcal{A}_1^e$ (%)	0.01 1.12	0.12 3.18	-10.78 -1.59
250.8	250.9	128	21	0.130 0.035	0.847 0.461	0.000 0.001
Pedersen				0.135 0.037	0.897 0.467	0.000 0.001
Cowling				0.160 0.033	1.146 0.419	0.000 0.002
$\overline{\sigma}$ = 0.6025 S/m			$\Delta\mathcal{A}_1^e$ (%)	-0.00 -0.00	-0.00 -0.00	-0.00 -0.00
$\sigma_{\rm top}$ = 0.6062 S/m			$\Delta\mathcal{A}_1^e$ (%)	0.08 -0.53	0.28 -0.34	1.23 0.61

Table S3. Callisto: Magnetic induction field strengths {Re,Im}($B_x\mathcal{A}_n^e$), in nT, at the main inducing periods in Figure 1. For the different ocean compositions and thicknesses of the upper ice I lithosphere/ocean ($D_{\rm I}/D_{\rm ocean}$; Figure 6), the adiabatic response is listed first. These values are also shown in Figure S6. Following these are the responses (in nT) including a 100 km ionosphere with {Pedersen,Cowling} conductance of {800,6850} S (Hartkorn & Saur, 2017), then the deviations from the adiabatic case (in %) for the ocean with uniform conductivity set to the mean of the adiabatic ocean ($\overline{\sigma}$), and then for the case with uniform conductivity set to the value at the ice–ocean interface ($\sigma_{\rm top}$). The surface responses of the ionosphere in the absence of an ocean are listed at the top of the table.

Europa			Period (hr):	**5.62**	**11.23**	**84.63**
			B_z (nT):	**1.22**	**15.24**	**11.97**
T_b (K)	$\overline{T}$ (K)	$D_{\rm I}$ (km)	$D_{\rm ocean}$ (km)		$B_z\mathcal{A}_1^e$ (nT)	
Ionosphere Only				**Re Im**	**Re Im**	**Re Im**
Pedersen				0.000 0.008	0.000 0.053	0.000 0.006
$MgSO_4$ 1 wt%				**Re Im**	**Re Im**	**Re Im**
273.1	273.9	5	117	1.104 0.124	13.409 2.771	3.339 5.049
Pedersen				1.105 0.124	13.412 2.772	3.342 5.052
$\overline{\sigma}$ = 0.4533 S/m		$\Delta\mathcal{A}_1^e$ (%)		0.36 -0.41	0.39 -0.08	0.85 0.50
$\sigma_{\rm top}$ = 0.4107 S/m		$\Delta\mathcal{A}_1^e$ (%)		0.10 7.75	-0.45 8.80	-12.31 -3.57
270.4	271.1	30	91	1.057 0.155	12.497 3.574	1.910 4.078
Pedersen				1.057 0.155	12.503 3.575	1.913 4.082
$\overline{\sigma}$ = 0.4132 S/m		$\Delta\mathcal{A}_1^e$ (%)		0.22 -0.10	0.24 0.01	0.55 0.34
$\sigma_{\rm top}$ = 0.3847 S/m		$\Delta\mathcal{A}_1^e$ (%)		-0.09 6.49	-0.88 6.09	-10.65 -4.23
$MgSO_4$ 10 wt%				**Re Im**	**Re Im**	**Re Im**
272.7	274.1	5	124	1.158 0.044	14.268 0.743	10.590 1.916
Pedersen				1.158 0.044	14.268 0.744	10.591 1.916
$\overline{\sigma}$ = 3.7646 S/m		$\Delta\mathcal{A}_1^e$ (%)		0.23 -3.83	0.33 -2.87	0.49 -0.10
$\sigma_{\rm top}$ = 3.3197 S/m		$\Delta\mathcal{A}_1^e$ (%)		-0.01 2.28	-0.01 2.13	-0.34 11.33
269.8	270.8	30	96	1.101 0.043	13.592 0.709	9.962 2.510
Pedersen				1.101 0.044	13.593 0.711	9.963 2.510
$\overline{\sigma}$ = 3.3661 S/m		$\Delta\mathcal{A}_1^e$ (%)		0.18 -2.30	0.23 -1.35	0.30 0.02
$\sigma_{\rm top}$ = 3.0763 S/m		$\Delta\mathcal{A}_1^e$ (%)		-0.01 1.41	0.08 2.77	-0.81 7.99
Seawater 0.35165 wt%				**Re Im**	**Re Im**	**Re Im**
274.9	275.7	5	117	1.101 0.134	13.285 3.017	2.893 4.833
Pedersen				1.101 0.134	13.289 3.018	2.896 4.836
$\overline{\sigma}$ = 0.4124 S/m		$\Delta\mathcal{A}_1^e$ (%)		0.41 -0.33	0.44 -0.04	0.96 0.58
$\sigma_{\rm top}$ = 0.3670 S/m		$\Delta\mathcal{A}_1^e$ (%)		0.05 9.74	-0.77 10.45	-15.30 -5.17
270.0	270.7	30	91	1.051 0.173	12.245 3.951	1.556 3.755
Pedersen				1.051 0.173	12.252 3.952	1.559 3.759
$\overline{\sigma}$ = 0.3651 S/m		$\Delta\mathcal{A}_1^e$ (%)		0.26 -0.07	0.29 0.03	0.65 0.42
$\sigma_{\rm top}$ = 0.3339 S/m		$\Delta\mathcal{A}_1^e$ (%)		-0.23 8.27	-1.49 7.33	-13.72 -5.87
Seawater 3.5165 wt%				**Re Im**	**Re Im**	**Re Im**
270.8	271.9	5	119	1.153 0.048	14.192 0.793	10.435 2.358
Pedersen				1.153 0.048	14.193 0.794	10.435 2.358
$\overline{\sigma}$ = 3.0760 S/m		$\Delta\mathcal{A}_1^e$ (%)		0.24 -3.32	0.33 -2.24	0.46 -0.03
$\sigma_{\rm top}$ = 2.7347 S/m		$\Delta\mathcal{A}_1^e$ (%)		-0.02 2.08	0.04 2.37	-0.74 10.53
268.2	269.1	30	91	1.095 0.045	13.555 0.760	9.695 2.979
Pedersen				1.095 0.046	13.556 0.762	9.696 2.979
$\overline{\sigma}$ = 2.8862 S/m		$\Delta\mathcal{A}_1^e$ (%)		0.18 -1.89	0.22 -0.95	0.28 0.03
$\sigma_{\rm top}$ = 2.6476 S/m		$\Delta\mathcal{A}_1^e$ (%)		0.01 1.46	0.10 3.88	-1.26 7.23

Table S4. Europa: Magnetic induction field strengths {Re,Im}($B_z\mathcal{A}_n^e$), in nT, at the main inducing periods in Figure 1. For the different ocean compositions and thicknesses of the upper ice I lithosphere/ocean ($D_{\rm I}/D_{\rm ocean}$; Figure 6), the adiabatic response is listed first. These values are also shown in Figure S6. Following these are the deviations from the adiabatic case (in %) for the responses including a 100 km ionosphere with Pedersen conductance of 30 S (Hartkorn & Saur, 2017), then for the ocean with uniform conductivity set to the mean of the adiabatic ocean ($\overline{\sigma}$), and then for the case with uniform conductivity set to the value at the ice–ocean interface ($\sigma_{\rm top}$). The surface responses of the ionosphere in the absence of an ocean are listed at the top of the table.

Ganymede			Period (hr):	**5.27**	**10.53**	**171.57**
			B_z (nT):	**1.78**	**2.42**	**0.38**
T_b (K)	$\overline{T}$ (K)	$D_{\rm I}$ (km)	$D_{\rm ocean}$ (km)		$B_z\mathcal{A}_1^e$ (nT)	
Ionosphere Only				**Re Im**	**Re Im**	**Re Im**
Pedersen				0.000 0.001	0.000 0.001	0.000 0.000
$MgSO_4$ 1 wt%				**Re Im**	**Re Im**	**Re Im**
270.7	279.0	25	442	1.618 0.101	2.137 0.188	0.248 0.122
Pedersen				1.618 0.101	2.137 0.188	0.248 0.122
$\overline{\sigma}$ = 0.5166 S/m			$\Delta\mathcal{A}_1^e$ (%)	0.87 -8.82	1.23 -7.04	2.61 1.01
$\sigma_{\rm top}$ = 0.3890 S/m			$\Delta\mathcal{A}_1^e$ (%)	-0.03 4.54	-0.14 5.86	-9.33 17.09
261.6	266.2	92	276	1.466 0.112	1.941 0.197	0.131 0.149
Pedersen				1.466 0.112	1.941 0.197	0.131 0.149
$\overline{\sigma}$ = 0.3322 S/m			$\Delta\mathcal{A}_1^e$ (%)	0.95 -5.29	1.18 -2.65	2.44 1.41
$\sigma_{\rm top}$ = 0.2623 S/m			$\Delta\mathcal{A}_1^e$ (%)	0.08 3.83	0.45 10.74	-22.82 -3.32
$MgSO_4$ 10 wt%				**Re Im**	**Re Im**	**Re Im**
270.2	278.3	25	458	1.690 0.038	2.274 0.071	0.320 0.039
Pedersen				1.690 0.038	2.274 0.071	0.320 0.039
$\overline{\sigma}$ = 4.0699 S/m			$\Delta\mathcal{A}_1^e$ (%)	0.29 -10.57	0.41 -9.78	1.48 -3.07
$\sigma_{\rm top}$ = 3.1150 S/m			$\Delta\mathcal{A}_1^e$ (%)	-0.00 2.03	-0.01 2.84	-0.18 7.55
260.0	263.5	93	282	1.548 0.045	2.077 0.085	0.294 0.051
Pedersen				1.548 0.045	2.077 0.085	0.294 0.051
$\overline{\sigma}$ = 2.3476 S/m			$\Delta\mathcal{A}_1^e$ (%)	0.27 -7.17	0.38 -6.43	1.01 -0.28
$\sigma_{\rm top}$ = 1.9483 S/m			$\Delta\mathcal{A}_1^e$ (%)	0.00 1.71	-0.00 2.51	-0.11 15.65
bottom layer: 30 km 20 S/m			$\Delta\mathcal{A}_1^e$ (%)	0.00 -0.00	0.00 -0.00	-1.20 0.20
Pedersen			$\Delta\mathcal{A}_1^e$ (%)	0.00 0.10	0.00 0.04	-1.20 0.20

Table S5. Ganymede: Magnetic induction field strengths {Re,Im}($B_z\mathcal{A}_n^e$), in nT, at the main inducing periods in Figure 1. For the different ocean compositions and thicknesses of the upper ice I lithosphere/ocean ($D_{\rm I}/D_{\rm ocean}$; Figure 6), the adiabatic response is listed first. These values are also shown in Figure S7. Following these are the deviations from the adiabatic case (in %) for the responses including a 100 km ionosphere with Pedersen conductance of 2 S (Hartkorn & Saur, 2017), then for the ocean with uniform conductivity set to the mean of the adiabatic ocean ($\overline{\sigma}$), and then for the case with uniform conductivity set to the value at the ice–ocean interface ($\sigma_{\rm top}$). The surface responses of the ionosphere in the absence of an ocean are listed at the top of the table.

Callisto			Period (hr):	**5.09**	**10.18**	**400.33**
			B_z (nT):	**1.82**	**0.20**	**0.14**
T_b (K)	$\overline{T}$ (K)	$D_{\rm I}$ (km)	$D_{\rm ocean}$ (km)		$B_z\mathcal{A}_1^e$ (nT)	
Ionosphere Only				**Re Im**	**Re Im**	**Re Im**
Pedersen				0.141 0.508	0.004 0.030	0.000 0.001
Cowling				1.677 0.708	0.130 0.110	0.000 0.005
$MgSO_4$ 1 wt%				**Re Im**	**Re Im**	**Re Im**
257.4	259.6	99	132	1.489 0.166	0.162 0.034	0.002 0.014
Pedersen				1.511 0.190	0.165 0.036	0.002 0.015
Cowling				1.683 0.265	0.181 0.039	0.003 0.019
$\overline{\sigma}$ = 0.2307 S/m			$\Delta\mathcal{A}_1^e$ (%)	0.49 -0.44	0.53 -0.08	1.45 0.96
$\sigma_{\rm top}$ = 0.1965 S/m			$\Delta\mathcal{A}_1^e$ (%)	0.06 14.62	-1.03 15.03	-26.08 -13.62
250.8	250.9	128	21	0.438 0.690	0.016 0.049	0.000 0.001
Pedersen				0.746 0.865	0.031 0.072	0.000 0.002
Cowling				1.738 0.603	0.148 0.102	0.000 0.006
$\overline{\sigma}$ = 0.0895 S/m			$\Delta\mathcal{A}_1^e$ (%)	0.04 0.02	0.04 0.03	0.05 0.03
$\sigma_{\rm top}$ = 0.0874 S/m			$\Delta\mathcal{A}_1^e$ (%)	-3.26 -0.99	-4.12 -1.87	-4.52 -2.28
$MgSO_4$ 10 wt%				**Re Im**	**Re Im**	**Re Im**
255.7	256.9	99	130	1.539 0.057	0.171 0.008	0.046 0.059
Pedersen				1.546 0.079	0.171 0.010	0.047 0.059
Cowling				1.648 0.195	0.177 0.018	0.049 0.060
$\overline{\sigma}$ = 1.5256 S/m			$\Delta\mathcal{A}_1^e$ (%)	0.20 -2.91	0.26 -1.74	0.69 0.39
$\sigma_{\rm top}$ = 1.3789 S/m			$\Delta\mathcal{A}_1^e$ (%)	0.01 1.12	0.12 3.18	-10.78 -1.59
250.8	250.9	128	21	1.420 0.386	0.132 0.072	0.000 0.006
Pedersen				1.476 0.399	0.140 0.073	0.000 0.006
Cowling				1.743 0.358	0.179 0.065	0.001 0.010
$\overline{\sigma}$ = 0.6025 S/m			$\Delta\mathcal{A}_1^e$ (%)	-0.00 -0.00	-0.00 -0.00	-0.00 -0.00
$\sigma_{\rm top}$ = 0.6062 S/m			$\Delta\mathcal{A}_1^e$ (%)	0.08 -0.53	0.28 -0.34	1.23 0.61

Table S6. Callisto: Magnetic induction field strengths {Re,Im}($B_z\mathcal{A}_n^e$), in nT, at the main inducing periods in Figure 1. For the different ocean compositions and thicknesses of the upper ice I lithosphere/ocean ($D_{\rm I}/D_{\rm ocean}$; Figure 6), the adiabatic response is listed first. These values are also shown in Figure S6. Following these are the responses (in nT) including a 100 km ionosphere with {Pedersen,Cowling} conductance of {800,6850} S (Hartkorn & Saur, 2017), then the deviations from the adiabatic case (in %) for the ocean with uniform conductivity set to the mean of the adiabatic ocean ($\overline{\sigma}$), and then for the case with uniform conductivity set to the value at the ice–ocean interface ($\sigma_{\rm top}$). The surface responses of the ionosphere in the absence of an ocean are listed at the top of the table.